Electroluminescence of Halide Perovskites with Potassium Passivation

*Anil Kanwat, Natalia Yantara, Yan Fong Ng, Thomas J. N. Hooper, Prem Jyoti Singh Rana, Benny Febriansyah, Padinhare Cholakkal Harikesh, Teddy Salim, Parth Vashishtha, Subodh G. Mhaisalkar, and Nripan Mathews**

Dr. A. Kanwat, Dr. N. Yantara, Dr. T. J. N. Dr. Hooper, Dr. P. J. S. Rana, B. Febriansyah, P. C. Harikesh
Energy Research Institute @ NTU, Nanyang Technological University, Research Techno Plaza, X-Frontier Block, Level 5, 50 Nanyang Drive, 637553, Singapore

Y. F. Ng, Dr. T. Salim, Dr. P. Vashishtha, Prof. N. Mathews, Prof. S. G. Mhaisalkar
School of Materials Science and Engineering, Nanyang Technological University, 50 Nanyang Avenue, 639798, Singapore
E-mail: Nripan@ntu.edu.sg

Keywords: halide perovskite, electroluminescence, halide migration, light emitting diode

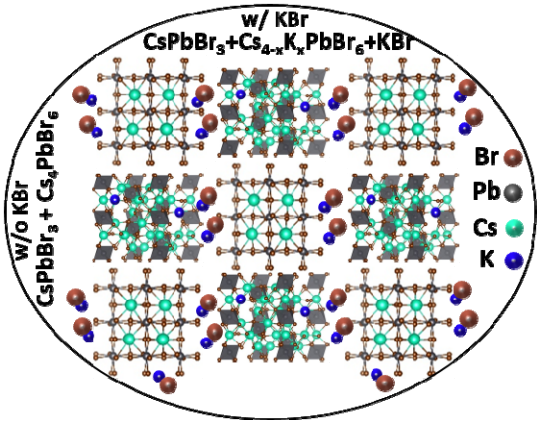

Halide perovskites are of great interest for light-emitting diodes (PeLEDs) in recent years due to their excellent photo- and electroluminescence properties. However, trap/defects and ion migration of devices under high external driving voltage/current are yet to be overcome. In this work, it is found that upon potassium (K) addition to a $CsPbBr_3$/$Cs4PbBr_6$ (3D:0D = 0.85:0.15) perovskite, a locally-disordered 0D $Cs_{4-x}K_xPbBr_6$ phase is formed with nearly 0.35:0.65 admixture of 0D:3D, along with an unreacted KBr phase potentially passivating the surface and grain boundaries. The formation of $CsPbBr_3$ nanocrystals (~10nm) confined within the $Cs_{4-x}K_xPbBr_6$ matrix accompanied by larger $CsPbBr_3$ grains (~50nm) is further confirmed by high-resolution transmission electron microscopy. In addition, the kinetics of ion migration were characterized with Auger electron spectroscopy and double-layer polarization using capacitive-frequency measurements, revealing significantly lower

hysteresis, halide ion migration and accumulation for the K-incorporated samples during device operation, resulting in substantial improvements in LED performances and stability.

1. Introduction

Halide perovskites are undergoing a rapid development for optoelectronic applications, particularly in solar cells (PSC)[1,2] and light-emitting diodes (PeLEDs).[3,4] The power conversion efficiencies (PCEs) of PSCs have recently been shown to exceed 25%,[5] while the external quantum efficiencies (EQEs) of PeLEDs exceeding 20% for both green and red, and 10% for blue have been reported within a short span of time.[6-8] However, the quest for stabilizing perovskite devices has been challenging and requires continuous investigation into different aspects of compositional chemistry for the perovskite compound. In particular, the stability of perovskite devices has been associated with moisture/heat instability of the A-site organic cation in the ABX_3 perovskite crystal structure (where A is a monovalent cation (methylammonium (MA^+), formamidinium (FA^+) or cesium (Cs^+)), B is a divalent cation (Pb^{2+}, Mn^{2+} or Zn^{2+}), and X is a halide anion (I^-, Br^- or Cl^-)), joule heating at operational bias, and halide ion migration.[9-18] Numerous approaches have been employed to remove joule heating by using thermally stable materials and to suppress ion migration by doping or mixing with poly(ethylene oxide) (PEO),[19,20] phenylethylammonium (PEA),[21] (9,9-bis(3-(N,N-dimethylamino)propyl)-2,7-fluorene)-alt-2,7-(9,9-dioctylfluorene) (PFN),[22] and 3,3-diphenylpropylamine bromide (DPPA-Br),[23,24]. Additionally, improving structural stability by substitution or doping of A- (MA^+, FA^+, Cs^+), and B- (Pb^{2+}, Mn^{2+}, Zn^{2+}, Ce^{3+}) site cations have been explored.[10-18] Various efforts have also been made in tuning the dimensionality of the perovskite by substituting the A-site cations with organic additives and long chain ammonium salts such as alkyl ammonium,[25] phenylethylammonium,[26-29] 1-naphthylmethylammonium,[30-32] and phenylbutylammonium[33] to improve the device performance. All-inorganic perovskites, having higher decomposition temperatures, also benefit from higher operational stability. Thus, studies have increasingly shifted towards

substituting or doping the A-site cation with alkali ones such as cesium (Cs^+), rubidium (Rb^+),[34-36] and potassium (K^+),[37-39] away from organic cations such as MA^+ and FA^+.

According to Goldschmidt's tolerance factor, for an all-inorganic halide perovskite, only Cs^+ can form stable perovskite structures when occupying the A-site of the crystal lattice, with the tolerance factor ($t = (r_A + r_X)/\left(\sqrt{2}(r_B + r_X)\right)$, where r is the ionic radius) falling in the eligible range between 0.8 and 1.[40-42] Indeed, previous reports found that Rb^+/K^+ ions do not incorporate into the 3D perovskite lattice. Instead, potassium complexes with bromide form a thin surface passivation layer while rubidium addition results in the formation of phase-segregated rubidium halide crystals.[37,43-46] Moreover, the presence of Rb^+/K^+ in perovskite precursors has been shown to improve the optoelectronic properties and moisture stability of perovskites[37,43-46]. The lifetime and PCE of triple cation CsFAMA PSCs with Rb^+ addition have been shown to increase to thousands of hours at elevated temperatures and 21.6%, respectively. Potassium addition effectively increases the grain size and reduces the interfacial defect density in the CsFAMA perovskite layer, leading to hysteresis-free, stable, and high PCE (20.56%) quadruple-cation PSCs.[47] Hence, defect passivation by small alkali cation in perovskites plays an essential role in the device performance, e.g., hysteresis, stability, and light emission. However, a systematic investigation of ion migration dynamics in cesium lead halide perovskites with K^+ addition, along with the effects on PeLED device stability, has not yet been explored. Unlike PSCs, which have thicker perovskite layers and work at the maximum power point, PeLEDs have thinner films and operate under higher external driving voltages and current, which intensify the built-in electric field during device operation. As a result, there is a much higher driving force for ion migration in PeLEDs which thus demands strategies to mitigate this effect in order to preserve the optoelectronic functions. Although both halide and A-site cation migrations have been observed in PSCs, halide migration has been identified as the major contributor of operational instability.[48,49]

In this study, we investigated the role of KBr-mixed 0D/3D perovskite admixture on defect passivation using X-ray diffraction (XRD), Auger electron spectroscopy (AES), solid-state nuclear magnetic resonance (ssNMR), and high-resolution transmission electron microscopy (HRTEM). ssNMR is thus far an underutilized technique for the study of lead halide perovskites, although recent reports have found it to be highly informative. Characterization of lead halide perovskites are mostly conducted in thin films or nanoparticle dispersions, and these systems often lack the long-range order necessary for analysis by more traditional techniques (i.e. diffraction). Conversely, the short-range, element-specific nature of ssNMR allows it to provide structural characterization even in highly disordered materials. A large portion of the current ssNMR literature in this field has been focused on the study of cation dynamics and molecular rotations in hybrid perovskites using the popular ^{1}H, ^{13}C and ^{14}N NMR experiments.[50-53] In addition, ^{207}Pb NMR has been proven to be useful in determining the phase composition of lead halide perovskites with mixed cations/anions.[51,52,54,55] Structural and phase characterization can also be provided for all-inorganic (i.e. Cs-based) perovskites via ^{133}Cs NMR, which benefits from greater sensitivity and a more accessible chemical shift range than ^{207}Pb NMR.[43,55,56] Furthermore, ssNMR correlation experiments have begun to be used to elucidate the interactions between the perovskite surface and surrounding ligands, which can play an important role in the optoelectronic properties of the system.[57] In this study, we have utilized ^{133}Cs, ^{207}Pb and ^{79}Br to elucidate the structural differences in the K^{+}-passivated perovskite.

Additionally, we explored the role of KBr mixed 0D/3D admixture perovskite light emitter layer, and investigated the mechanism of ion migration in the corresponding PeLED device. To understand the mechanism of ion migration and its role in the devices' electroluminescence (EL) stability, electrical poling and double-layer polarization of these K^{+}-doped perovskite devices have been thoroughly examined.

2. Results and Discussion

The unmodified 0D/3D admixture perovskite solution was prepared by mixing CsBr and $PbBr_2$ precursor in dimethyl sulfoxide (DMSO) to a total concentration of 0.3 M with CsBr:$PbBr_2$ ratio fixed at 1.2:1. Three KBr modified solutions were then prepared by mixing 0.3 M $CsPbBr_3$ and 0.3 M KBr solutions in v/v ratios of 100:0, 90:10, 80:20, and 70:30. KBr mixed 0D/3D films prepared in this manuscript for optical, structural, and device characterizations have the same reference and are coated on indium tin oxide (ITO) / poly(3,4-ethylenedioxythiophene) polystyrene sulfonate (PEDOT:PSS) substrates. For easier reference, KBr mixed 0D/3D admixture thin films prepared from 0D/3D:KBr v/v ratio of 100:0, 90:10, 80:20, and 70:30 will be denoted as K0, K10, K20, and K30, respectively. **Fig. 1a** shows the XRD patterns of each film. The diffraction pattern peaks at 15.2, 21.4, and 30.36° can be indexed to the pure $CsPbBr_3$ orthorhombic phase of (101), (121), and (202) planes, respectively.[28] Additional XRD peaks were observed upon KBr incoportation at 13.04 and 29.48°, which are assigned to the (110) and (214) planes of Cs_4PbBr_6, respectively, while the peak at 26.38° can be indexed to the (111) plane of KBr. This reveals that mixing KBr in $CsPbBr_3$ results in the formation of three phases; Cs_4PbBr_6 (0D perovskite), $CsPbBr_3$ (3D perovskite), and KBr. The diffraction peaks for K10 marginally shifts by 0.02° to a lower angle (30.34°) as shown in the zoomed-in (202) plane in **Fig. 1b.** Further doping in the K20 and K30 films do not observe any additional shift in the diffraction peak. We believe that this minute shift in the XRD pattern is within experimental error, and thus the structure is assumed to be unchanged upon K^+ doping.[37,38,58]

Fig. 1c shows the ultraviolet-visible (UV-vis) absorbance onset and the photoluminescence (PL) spectra of K0, K10, K20 and K30 thin films. The optical bandgap of $CsPbBr_3$ derived from the absorbance onset shifts slightly from 2.36 eV (K0) to 2.34 eV (K30) upon K^+ incorporation. A recent study by Cao et al. shows a similar observation in a mixed halide,

$Cs_{0.11}MA_{0.15}FA_{0.74}Pb(Br_{0.17}I_{0.83})_3$ perovskite system.[36] Similarly, the PL peak red shifts from 523 nm (K0) to 526 nm (K30). Fig. S1a depicts the PL intensity enhancement of films with various KBr addition. In addition, PL quantum yield (PLQY) of the films (Fig. S1b and c) are enhanced by 3.5 times upon 20% KBr addition (K20), implying that KBr plays an important role in defect passivation. In both cases (K0 and K20), PL intensity and PLQY remain fairly constant after 90 h storage in 30% relative humidity (RH), indicating excellent PL stability under moisture for the fully-inorganic perovskite system. While the absorbance onset and PL peak are slightly red-shifted from K0 to K20, no evidence of incorporation is observed from the XRD. Therefore, ssNMR was performed on powder samples of K0 and K20 to confirm the state of elemental interaction in the perovskite lattice. The powder of these two samples were prepared via drop casting the perovskite precursors on bare glass and scraping multiple films after drying on a hot plate at 70 °C.

Fig. 1d-f show the ^{133}Cs, ^{207}Pb and ^{79}Br magic angle spinning (MAS) NMR spectra. Both ^{133}Cs MAS NMR spectra of K0 and K20 present two resonances which correlate to the Cs environments in a $CsPbBr_3$ phase (δ_{iso} = 118 ppm) and in a 0D Cs_4PbBr_6 phase (δ_{iso} = 236 ppm). Although the XRD pattern of the unmodified film (K0) does not show presence of the 0D peak, it is likely that the 0D phase is in trace amounts and undetected. On the other hand, the addition of potassium appears to enhance the formation of the 0D phase. The ^{133}Cs NMR spectra were fitted with Gaussian/Lorentzian line shapes, providing the NMR parameters given in Table S1, which match the previously reported values for these two perovskite (0D and 3D) phases.[55] The spectral simulation gives $CsPbBr_3$:Cs_4PbBr_6 ratios of 85:15 and 65:35 for the K0 and K20 samples, respectively. The resonance of the $CsPbBr_3$ perovskite phase is identical between the K0 and K20 spectra (δ_{iso} = 117.6 ± 0.6 ppm; FWHM = 0.36 ± 0.04 kHz), hence it is unlikely that the K^+ ions are integrated into the 3D perovskite lattice. Conversely, the Cs_4PbBr_6 resonance is significantly broader in K20, with a FWHM of roughly

4 times larger than the analogous resonance in K0. This broadening is indicative of a distribution of Cs environments in a locally disordered 0D perovskite phase inferring partial K^+ substitution/occupation.[44] The bulk observing nature of NMR confirms that the K^+ is not only acting at grain boundaries or surface sites, but also produces disorder in the 0D perovskite lattice as a whole.

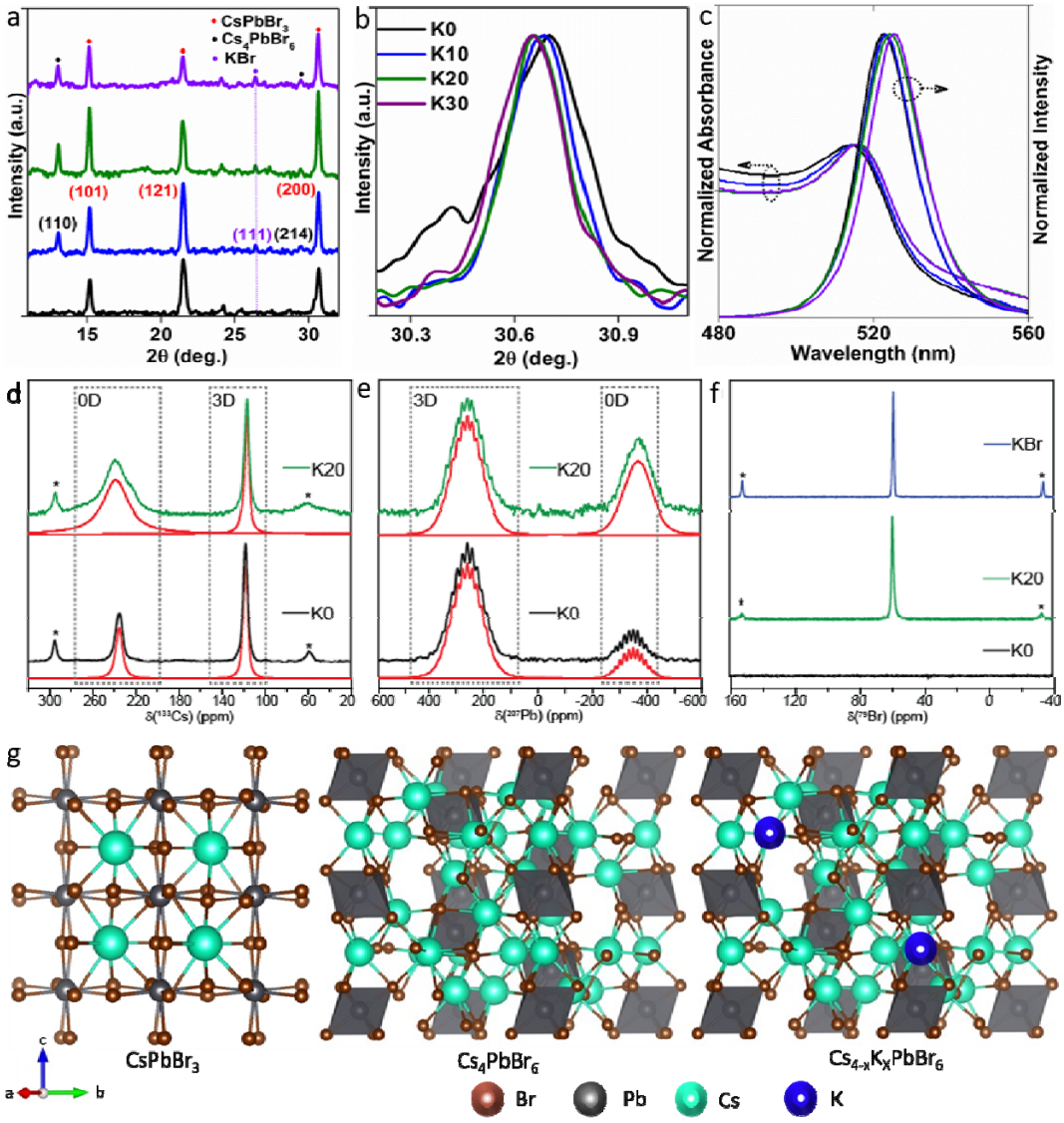

FIG. 1 XRD diffraction patterns of each KBr-mixed 0D/3D perovskite films with increasing KBr concentration; K0, K10, K20, and K30. (a) Full scan and (b) zoomed-in on the (202) plane (normalized). (c) Normalized absorbance and photoluminescence spectra of perovskite films with increasing KBr concentration. Solid state (d) ^{133}Cs, (e) ^{207}Pb and (f) ^{79}Br NMR spectra of unmodified (K0) and modified (K20) perovskite thin film powders. Deconvolved resonances of the simulated NMR line-shapes are shown in red and spinning sidebands are marked by asterisks (*). (g) Schematic of lattice distortion upon K^+ incorporation into an orthorhombic $CsPbBr_3$ lattice.

The findings of the ^{133}Cs NMR data are corroborated by the ^{207}Pb MAS NMR spectra of the K0 and K20 samples (**Fig. 1e**). Similarly, both ^{207}Pb MAS NMR spectra present two resonances assigned to the 3D and 0D perovskite phases.[55] The line shapes of the resonances in sample K0 both display a fine structure as a result of Pb-Br scalar coupling. This coupling between Pb and the six quadrupolar Br nuclei (nuclear spin of 3/2) in the octahedral units of both phases, results in the splitting multiplets observed. By simulating the scalar coupling line shapes (see **Fig. 1e)**, J^1(^{207}Pb-$^{79/81}$Br) values of 2.3 ± 0.3 and 2.0 ± 0.2 kHz were obtained for the 3D and 0D phase, respectively. These values are in agreement with the limited existing reports of ^{207}Pb scalar coupling in lead bromide perovskites.[51,56] The full ^{207}Pb NMR parameters determined via spectral simulation are given in Table S2. In sample K20, the NMR parameters of the $CsPbBr_3$ resonance (δ_{iso} = 270 ± 3 ppm) is closely matching (within error) those of K0. The Cs_4PbBr_6 resonance, however, has shifted (from -349 to -366 ppm) and the scalar coupling fine structure is no longer present, presumably due to broadening of the individual spikelets. Analogous to the ^{133}Cs NMR data, this can be explained by the local disorder within the 0D perovskite lattice.

In addition, ^{79}Br MAS NMR was performed on both samples and the spectra are shown in **Fig. 1f**. Due to the large quadrupole moment of ^{79}Br, detection of ^{79}Br NMR resonances in the asymmetric Br environment in perovskites is difficult. However, the cubic symmetry of KBr results in negligible electric field gradients, nullifying the quadrupolar interaction, allowing the KBr resonance to be easily observed with ^{79}Br NMR. By comparing the ^{79}Br NMR spectra of K20 and pure KBr, it is clear that a KBr phase is present in the K20 sample, corroborating the XRD results. The confirmed presence of unreacted KBr opens up the possibility of surface/grain boundary passivation of both perovskite phases, alongside the observed incorporation of K^+ into the 0D perovskite phase.[43] **Fig. 1g** depicts the schematic of 3D, 0D, and K incorporated 0D phase.

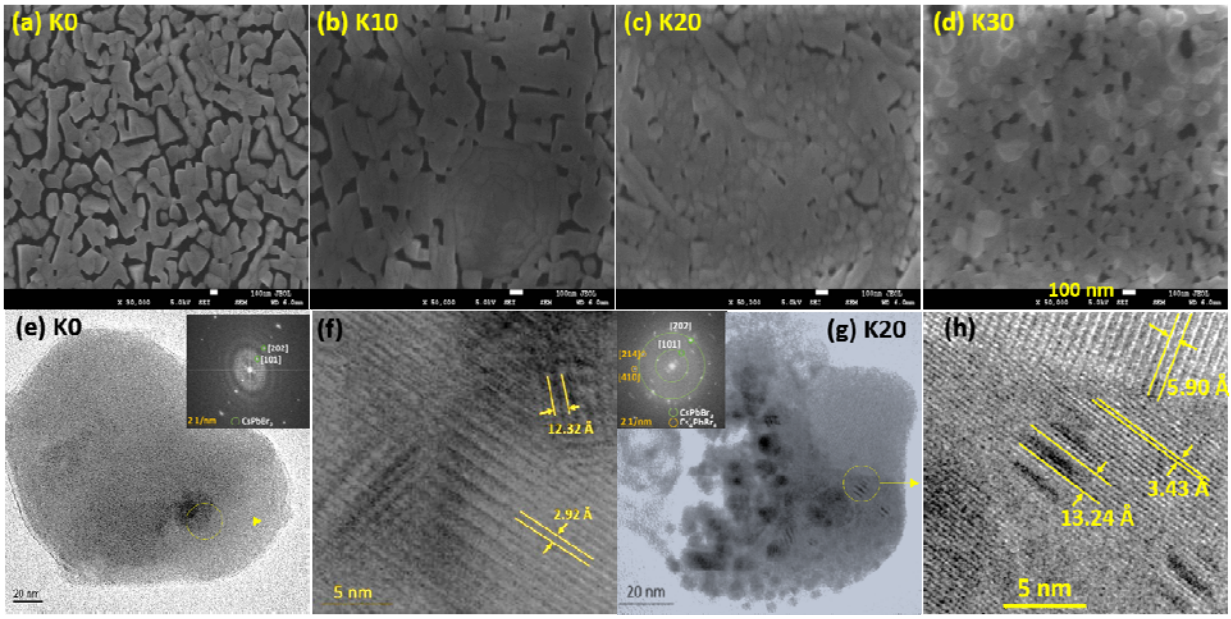

FIG. 2 Field emission scanning electron microscopy of samples with increasing KBr concentration in an admixture of 0D/3D; (a) K0, (b) K10, (c) K20, and (d) K30 films, and high-resolution transmission electron microscopy of (e,f) K0, and (g-h) K20 films. The insets in (e) and (g) show the SAED pattern of each respective film.

The field emission scanning electron microscopy (FESEM) image of the K0 sample shows large and non-uniform grains with visible pinholes (**Fig 2a**). With increasing KBr concentration however, the average grain size reduces from 193 nm to 118, 65, and 55 nm for K10, K20, and K30 films, respectively (deduced from the Gaussian fit on particle size of each SEM image as shown in the histogram of Fig. S2). K20 shows an optimum compact morphology with minimum pinholes (**Fig 2c**), while further KBr addition (K30) leads to an increased pinhole density with decreased crystallite size and rougher morphology (**Fig 2d**). This morphological evolution can be explained by the fact that the K^+ ion does not substitute Cs^+ inside the 3D lattice of $CsPbBr_3$, but contributes to either the formation of locally disordered mixed Cs/K 0D perovskite or secondary KBr phase that surround the 3D crystallites. As a result, the growth of 3D perovskite grains becomes inhibited with increasing K^+, resulting in smaller grains and smoother films. The addition of K^+ can also induce more nucleation sites which result in grain size reduction. These morphological refinements (i.e.

lower pinhole density) facilitate better charge injection and improve device performances as discussed subsequently.

To get a better insight on the morphological and structural changes upon KBr addition, we carried out transmission electron microscopy (TEM) along with selected area electron diffraction (SAED). **Fig. 2e-h** show the resulting TEM images of K0 and K20 samples. While K0 shows a typical orthorhombic $CsPbBr_3$ perovskite phase with large grain sizes of about 180 nm, K20 depicts two different perovskite crystallite sizes of 9-10 nm and 45-50 nm. The insets in **Fig. 2e and g** show the SAED patterns, and the magnified images in **Fig. 2f and h** depict the lattice fringes of the K0 and K20 samples. The multiple lattice spacings observed in the K20 sample, indicative of different perovskite phases, can be assigned to 3D (0.590±0.1 nm), 0D (0.343±0.1 nm), and a Moiré fringe pattern (1.324±0.1 nm) resulting from the overlapping of two lattice fringes. Mixing of the lattice fringes of the matrix (0D) with the lattice of the 3D phase was previously observed by Quan et al.[59] and others where they claim the formation of an admixture of 3D $CsPbBr_3$ nanocrystals (NCs) embedded in a rhombic prism hexabromide 0D Cs_4PbBr_6 microcrystals.[59-61] However, high electron beam currents applied to perovskite sample can potentially generate nanostructured artefacts.[62,63] To minimize this, we exposed specimen for barely 10 sec (lesser than 60s noted for observable beam damage in our samples) as shown in Fig. S3. The SAED results evidence the coexistence of 0D and 3D NC phases within the crystal, along with the polycrystalline 3D perovskite phase. Interestingly, K0 shows a pure 3D lattice fringe (0.292 nm) and an overlapped lattice fringe of 3D/0D (1.232 nm), and the proportion of 0D phase is significantly lower than that of K20 samples. Additionally, we did not observe confined 3D NCs in the K0 film from the TEM image. These findings are consistent with the XRD and ssNMR results, which show that KBr incorporation assists the formation of the 0D perovskite phase. However, TEM did not show the presence of a KBr phase, which indicates that this KBr

phase is most likely residing on the grain boundaries. For further verification, elemental mapping using AES (Fig. S4) has been performed, which indicated the absence of microcrystalline KBr and revealed a uniform distribution of K^+ throughout the sample within the resolution of the mapping system (~100nm). This indicates that the two phases identified in the ssNMR are uniformly distributed with nanocrystalline KBr possibly present at the grain boundaries / surface of perovskite as previously reported in the litreacture.[37-39, 43-45]

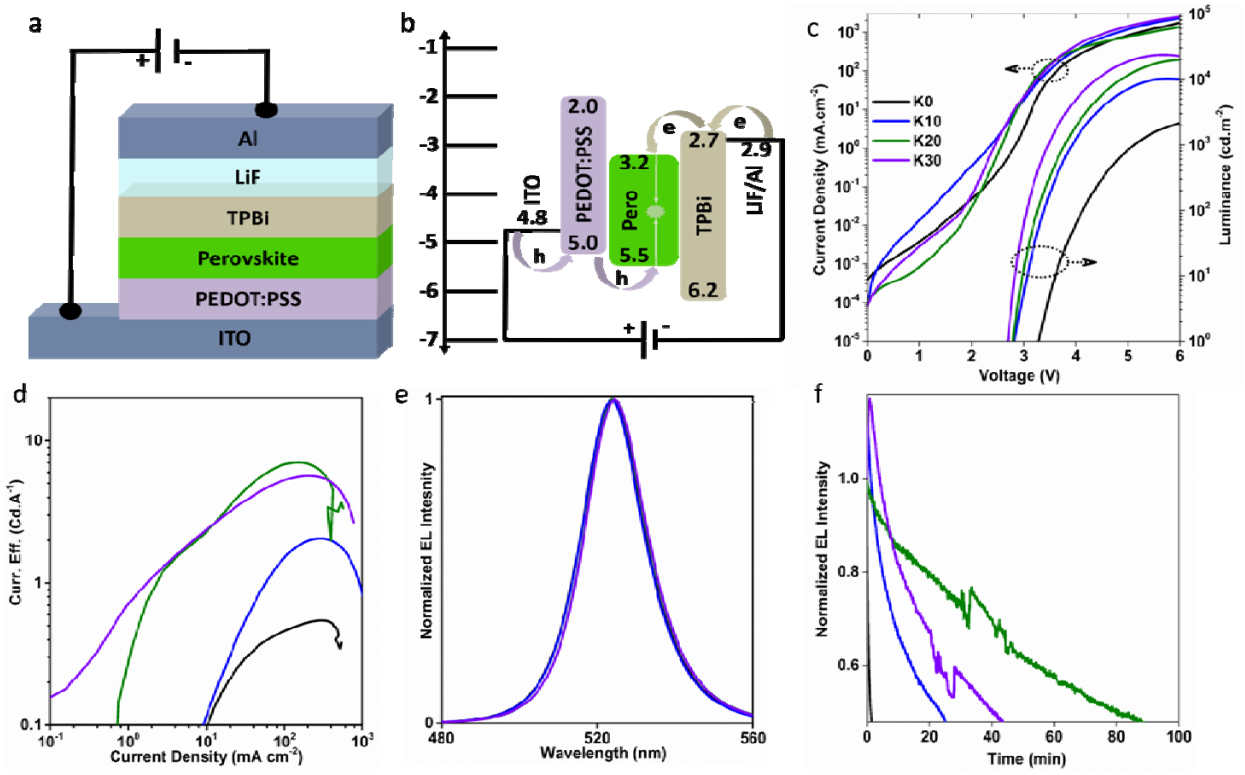

FIG. 3 (a) Device architecture and (b) energy levels of the PeLEDs adopted in this work. (c) J-V-L, (d) current efficiency, (e) EL spectra, and (f) EL stability of PeLEDs with increasing KBr concentration in an admixture of 0D/3D; K0, K10, K20, and K30.

Fig. 3a-c illustrate the device architecture, energy band levels and the resultant current density–voltage–luminance (*J–V–L*) plots of KBr-mixed 0D/3D PeLEDs using the following device architecture: ITO/PEDOT:PSS(40nm)/Perovskite(100nm)/TPBi(45nm) /LiF(0.8nm)/ Al(100nm). **Fig. 3d-f** depict the current efficiency, EL spectra, and EL stability of K0, K10, K20, and K30 PeLEDs. Notably, the J-V-L plots show an approximately ten-fold enhancement in maximum luminance from 2249 to 10205, 19785, and 23480 cd m^{-2}, and

reduction in turn on voltage from 3.3 to 2.9, 2.8, and 2.7 V with increasing KBr concentration from K0 to K10, K20, and K30, respectively. The turn on voltage indicates the lowest voltage required for radiative recombination in the device, usually defined as the voltage at which luminance reaches 1 cd m^{-2}. The low turn on voltage in K10, K20, and K30 devices indicate that K^+ addition enhances the radiative recombination by physically passivating the defects. Additionally, energy can funnel from 0D to confined 3D NCs and larger 3D domains which will contribute in total emission enhancement of the films as the emission range of 3D NCs overlaps with the larger 3D perovskite region.[59-61] Similarly, current efficiency and EQE values escalate rapidly from 0.54 to 2.06, 7.03, and 5.64 cd A^{-1}, and 0.14 to 0.53, 1.78, and 1.45%, as K^+ increases from K0 to K10, K20, and K30, respectively (Fig. 3d and Fig. S5a). The substantial enhancement in EL performances upon K^+ incorporation is attributed to the combinatorial effects of defect passivation, confinement of the 3D perovskite phase in the 0D matrix, along with improved film morphology (i.e. less pinhole density). Concomitantly, grain size reduction of the 3D NCs in the 0D matrix also improves the spatial confinement of injected charge carriers, and facilitates the formation of a compact film, resulting in reduced leakage current in the K20 device. At a higher KBr concentration (K30), a low turn on voltage and high brightness were observed but with poorer efficiencies, indicating electrical losses due to an increase in the pinhole density as shown from the SEM images (**Fig. 2d**). The EL spectrum of the K0 device shows a sharp emission peak centered at 524 nm, which shifts to 526 nm upon K-incorporation (K20), similar to that observed in the PL spectra. Additionally, the narrow and stable EL spectra of each KBr–modified devices (K10, K20, and K30) enable high color purity. The resultant full width at half maximum (FWHM) of the EL spectra saw a reduction from 20 nm (K0) to 18 nm (K20). The Commission Internationale de l'éclairage (CIE) coordinates of the K0 and K20 devices are (0.18, 0.82) and (0.14, 0.77), respectively, indicating a purer green emission for the KBr-modified PeLED (90.8%, **Fig. S5b**). **Fig. 3f** illustrates the EL stability of K0, K10, K20, and K30 devices observed at constant current and

an initial luminance of 100 cd.m^{-2}. The K0 PeLED device degrades to 50% of its initial luminance in about 3 min. Notably, the KBr-modified PeLEDs (K10, K20, and K30) exhibit half-lifetimes (T_{50}) of 25, 90, and 42 min, respectively. A thirty-fold enhancement in device stability with K20 confirms the superior passivation of grain boundaries and surface defects by the K^+ ions. Our practice of PeLED device testing has addressed each of the point on the checklist for reporting new LED materials published recently,[64] which presented a very clear guideline and standardized measurement protocol allowing for easier comparison across publications.

Importantly, the instability of PeLEDs can be associated with ionic migration, which triggers ion accumulation and formation of injection barriers at the interfaces. To investigate the potential effect of the 0D/3D admixture and KBr-passivated perovskite films on reducing the ion migration in PeLEDs under operation, the hysteresis of the devices were measured. We tracked the hysteresis of K0, K10, K20, and K30 samples under constant applied biases of 1, 2, and 3 as shown in **Fig. 4a and Fig. S6**. Prior to a full scan from 0 to 5 V, each device was given a polarization time of 1 min at each poling voltage. The electrical poling at lower (<1 V), and higher biases (2-3 V, before turn on voltage of the devices) were done to fill the shallow and deep traps, respectively. **Fig. 4a** illustrates the number of fold enhancement in the current density at 1 V (i.e. before current turn on / leakage current) before and after electrical poling at different biases. Each device was first polarized at 1 V with a polarization time of 1 min, and then reset to 0V for another 1 min. This cycle was repeated for five times before collecting the J-V, and then increased to 2 V and 3 V, subsequently. Current density of the K0 sample increases to about 40, 100, and 500 folds under a constant applied poling bias of 1, 2, and 3 V, respectively.

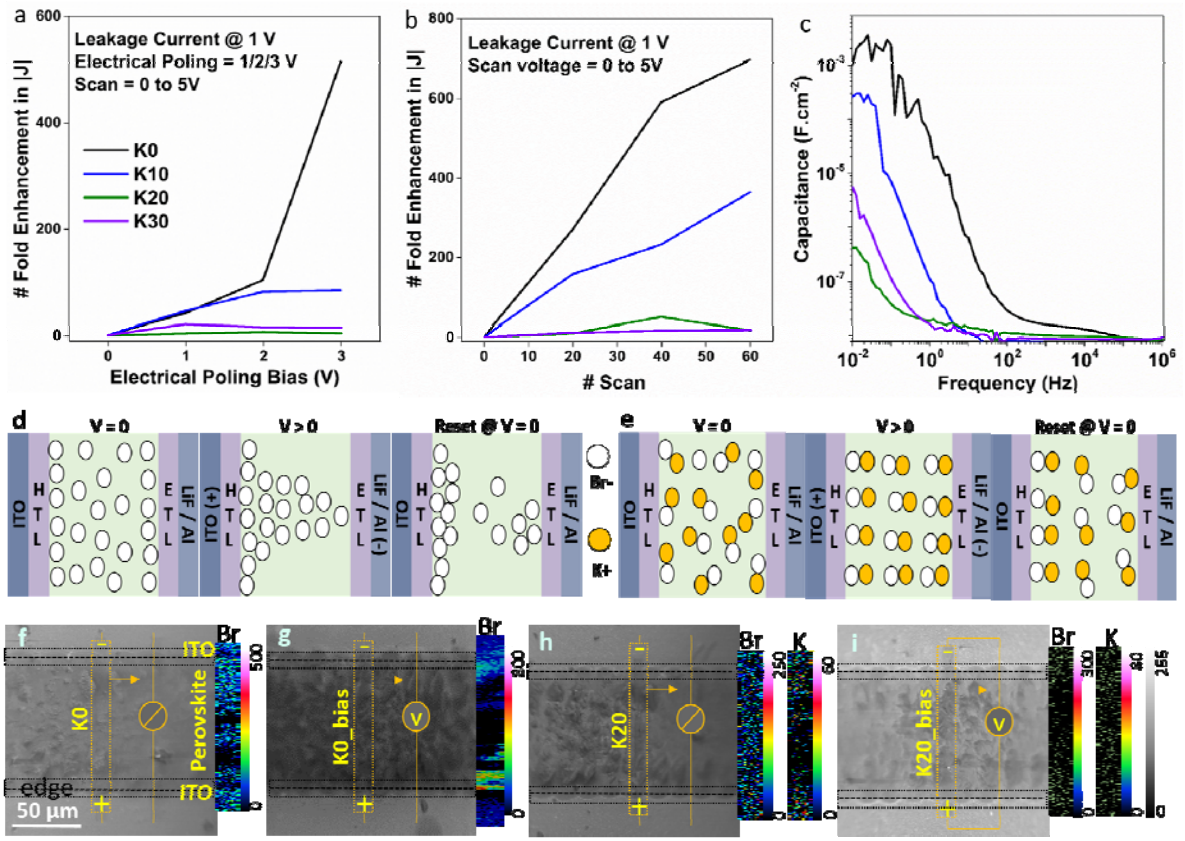

FIG. 4 (a) The number of fold enhancement in the current density @ 1 V after electrical poling at 1 V, 2 V, and 3 V. (b) The number of fold enhancement in the current density @ 1 V with multiple scans from 0-5 V. (c) Capacitance-frequency plot of impedance spectroscopy carried out on each K-doped device with increasing KBr concentration. Schematic representation of ion migration under static bias in (d) K0 and (e) K20 PeLED devices. Auger electron spectroscopy images and elemental mapping of (f,g) K0 and (h,i) K20 perovskite films before (f,h) and after (g,i) applied bias.

This indicates that electrical polarization even at a small bias (1 V) can severely degrade the device by creating shunt paths on the devices. With a small amount of KBr mixing, the K10 devices remarkably reduce the current gain to 40, 85 and 95 folds at 1, 2, and 3 V, respectively. The current gain reduces further to just 10 fold, and 20 fold in the K20 and K30 devices at 3 V, respectively, showing that the effect of electrical poling reduces remarkably on the electrical properties of the KBr-mixed devices. **Fig. 4b and S7** show the number of fold enhancement in the current density at 1 V with multiple scans from 0 to 5 V, which also takes into consideration the heating effect. Here, the current gain after 60 scan cycles decreases from 700 to 350, 20 and 30 folds with increasing KBr concentration from K0 to K10, K20, and K30, respectively. These results are consistent with the EL stability of the K0

and KBr-mixed PeLEDs (**Fig. 3f**), underlining the important role of K^+ doping in maintaining the device integrity.

It is hypothesized that shunt paths are caused by the creation of defects due to ion migration and/or extended ion accumulation at the interface and through the bulk emitter layer.[37] To study the ion accumulation at the external interfaces and the double-layer polarization of the electrode, capacitive techniques have been explored.[49,65] **Fig. 4c** depicts the capacitance-frequency plots of K0, K10, K20, and K30 devices under zero applied direct current (DC) bias and a modulated alternating current (AC) voltage perturbation. Above 100 Hz, all devices show low capacitance due to the lack of time for ions to migrate. At low frequency (10 mHz) however, K0, K10, K20, and K30 devices show capacitance in the range of 1000, 200, 0.5, and 6 $\mu F.cm^{-2}$, respectively. The high capacitance observed in the K0 device is ascribed to ion migration and accumulation that creates a double layer polarization at the interfaces. The remarkable reduction in the measured capacitance with K^+-doping (> 3 orders of magnitude) confirms its role in suppressing ion migration and accumulation at the interfaces, which is in direct agreement with the improved operational stability of the KBr-modified 0D/3D admixture devices. In a forward bias poling, when a positive voltage is applied to the ITO electrode in the K0 film, negatively charged Br^- ions migrate towards the grain boundaries or the hole transporting layer (HTL) interface. Migration of Br^- ions leads to a reservoir of halide vacancies in the perovskite layer accumulating from the interface of the electron transporting layer (ETL) to the HTL interface, as illustrated in **Fig. 4d**. Ion accumulation at the interfaces and grain boundaries modifies the built-in field, which results in current gain in the electrically-polarized devices (Fig. 4a-c, Fig. S6, S7). In the KBr-mixed perovskites however, the presence of the secondary phase (KBr) impedes the movement and migration of the ions as illustrated in **Fig. 4e**, which leads to significantly lower capacitance and current gain in these devices. Furthermore, Auger electron spectroscopy (AES) was performed on K0 and

K20 films before and after the constant applied bias to investigate the movement of ions. Fig. S8a shows the current plot under a constant applied bias of 200 V for 150 s. The K20 film shows a constant low current while the K0 film shows current gain with time at a static applied bias, suggesting formation of conductive shunt paths in a pure Cs system due to ionic migration. Fig. S8b shows the presence of Cs^+, Br^- and K^+ in the AES spectra and Fig. S8c-f show the elemental mapping of Cs in both the films before and after applying bias. Prior to the applied static bias, the Cs element is uniformly distributed across the film. However, after applying the bias, the Cs element starts to agglomerate towards the negative electrodes. On the contrary, although the Cs intensity is low due to partial substitution of K^+ in the K20 film, its elemental distribution remains unchanged after applying bias, implying that doping with K^+ stabilizes the perovskite phase and impedes ion migration. Similar results are observed from the Br^- and K^+ elemental mapping as shown in **Fig. 4f-i.** The initial uniformly distributed Br^- ions in the $CsPbBr_3$ sample drifted towards the positive electrode interfaces after the static applied electric field. It is to be noted that the solution-processed perovskites were spread across the top of the electrode and the channel. However, upon KBr mixing, the Br^- ion migration is significantly reduced as shown in the uniformly distributed Br^- mapping in **Fig. 4h and i**, confirming that the incorporation of K^+ largely suppresses ion migration upon the formation of an admixture of 0D and 3D phases along with the passivation of 3D perovskite with KBr.

3. Conclusion

In summary, we have explored the effect of mixing KBr in a 0D/3D admixture perovskite on the optoelectronic properties and PeLED performances, and investigated its role in ion migration. The results from HRTEM, ssNMR, and AES reveal that KBr-modified 0D/3D admixture leads to the formation of a locally disordered Cs/K 0D ($Cs_{4-x}K_xPbBr_6$) phase, which exists in a 0.35:0.65 admixture with the 3D phase, and an unreacted KBr phase which

is speculated to passivate the surface/defect sites of the 3D perovskite. The resultant KBr-passivation and the formation of 0D/3D admixture improves the PeLED efficiencies by fourteen-fold and stability by thirty-fold as compared to the unmodified device. The halide ion migration under an applied electric field appears to be the main cause of device instability in an unmodified device due to creation of additional shunt pathways and leakage channels. Additionally, with experimental evidences from electrical poling and capacitance-frequency measurement, we established that the K-doped samples largely suppress ion migration and accumulation, which opens up an important path towards more stable devices for practical applications.

4. Experimental Section

Perovskite preparation: $CsPbBr_3$ perovskite solution was prepared by mixing CsBr (Aldrich, 99.9%) and $PbBr_2$ (TCI Chemicals) in dimethyl sulfoxide (DMSO) to a concentration of 0.3 M and stirred overnight. The KBr mixed $CsPbBr_3$ solutions were prepared by mixing the as-prepared $CsPbBr_3$ solution and 0.3 M KBr solution in different v/v ratios of 90:10 (K10), 80:20 (K20), and 70:30 (K30).

Device fabrication: PeLED devices were fabricated on indium-doped tin oxide (ITO, 7 $\Omega \cdot cm^{-2}$) coated glass substrates. The substrates were cleaned by successive bath sonication in decon soap, deionized water, acetone, isopropanol and ethanol. They were then dried and treated in oxygen plasma for 30 min. Poly(3,4-ethylenedioxythiophene)-poly(styrenesulfonate) or PEDOT:PSS (Clevios P VP AI 4083) was spin-coated on the cleaned substrates at 4000 rpm for 60 s and annealed at 130°C for 30 min to remove any residual water. The perovskite films were deposited in an argon-filled glove box by spin coating the prepared solutions at 5000 rpm for 30 s on the PEDOT:PSS coated ITO substrate. Thereafter, the films were left to dry for 30 mins at ambient temperature before placing in a thermal evaporator. 1,3,5-Tris(1-phenyl-1-H-benzimidazol-2-yl)benzene or TPBi (LumTec,

sublimed > 99.5%) (45 nm) and cathode (LiF (0.8 nm) / Al (100 nm)) were thermally evaporated at a base pressure of $< 3 \times 10^{-6}$ Torr to complete the process of device fabrication. The devices were finally encapsulated inside the glove box. The final cell size was measured to be 8 mm^2.

Acknowledgements

This research was funded by National Research Foundation, Prime Minister's Office, Singapore under its Competitive Research Programme (CRP Award No. NRF-CRP14-2014-03), the Intra-CREATE Collaborative Grant (NRF2018-ITC001-001), and Ministry of Education Tier 2 project (MOE2018-T2-2-083). The auger electron microscopy work was performed at the Facility for Analysis, Characterization, Testing and Simulation (FACTS), Nanyang Technological University, Singapore.

References

(1) Miyata, A; Mitioglu, A.; Plochocka, P.; Portugall, O.; Wang,J. T. W..; Stranks, S. D.; Snaith, H.; Nicholas, R. J. Direct measurement of the exciton binding energy and effective masses for charge carriers in organic-inorganic tri-halide perovskites. *Nat. Phys.* **2015**, 11, 582-587.

(2) Yang, W. S.; Noh J. H., Jeon N. J., Kim Y. C., Ryu S., Seo J., Seok S. I. High-performance photovoltaic perovskite layers fabricated through intramolecular exchange. *Science.* **2015,** 348, 1234.

(3) Cho, H.; Jeong, S. H.; Park, M. H.; Kim, Y. H.; Wolf, C.; Lee, C. L.; Heo, J. H.; Sadhanala, A.; Myoung, N. S.; Yoo, S.; Im, S. H.; Friend, R. H.; Lee, T. W. Overcoming the electroluminescence efficiency limitations of perovskite light-emitting diodes. *Science.* **2015,** 350, 1222-1225.

(4) Tan, Z. K. Moghaddam, R. S.; Lai, M. L.; Docampo, P.; Higler, R.; Deschler, F.; Price, M.; Sadhanala, A.; Pazos, L. M.; Credgington, D.; Hanusch, F.; Bein, T.; Snaith, H. J.; Friend, R. H. Bright light-emitting diodes based on organometal halide perovskite. *Nat. nanotech.* **2014**, 9, 687-692.

(5) https://www.nrel.gov/pv/cell-efficiency.html

(6) Chiba, T.; Hayashi, Y.; Ebe, H.; Hoshi, K.; Sato, J.; Sato, S.; Pu, Y.-J.; Ohisa, S.; Kido, J. Anion-Exchange Red Perovskite Quantum Dots with Ammonium Iodine Salts for Highly Efficient Light-Emitting Devices. Nat. Photonics 2018, 12 (11), 681−687.

(7) Cao, Y.; Wang, N.; Tian, H.; Guo, J.; Wei, Y.; Chen, H.; Miao, Y.; Zou, W.; Pan, K.; He, Y.; et al. Perovskite Light-Emitting Diodes Based on Spontaneously Formed Submicrometre-Scale Structures. *Nature* **2018**, 562 (7726), 249−253.

(8) Wang, Q.; Wang, X.; Yang, Z.; Zhou, N.; Deng, Y.; Zhao, J.; Xiao, X.; Rudd, P.; Moran, A.; Yan, Y.; Huang, J.; Efficient sky-blue perovskite light-emitting diodes via photoluminescence enhancement. *Nat. Commun.* **2019**, 10, 5633.

(9) Zou, S.; Liu, Y.; Li, J.; Liu, C.; Feng, R.; Jiang, F.; Li, Y.; Song, J.; Zeng, H.; Hong, M.; Chen, X. Stabilizing cesium lead halide perovskite lattice through Mn(II) substitution for air-stable light-emitting diodes, *J. Am. Chem. Soc.* **2017**, 139, 11443-11450.

(10) Xu, W.; Li, F.; Lin, F.; Chen, Y.; Cai, Z.; Wang, Y.; Chen, X.; Synthesis of CsPbCl3-Mn nanocrystals via cation exchange, *Adv. Opt. Mater.* **2017**, 5, 1700520.

(11) Stam, W. van der; Geuchies, J. J.; Altantzis, T.; Bos, K. H. van den; Meeldijk, J.D.; Aert, S. V.; Bals, S.; Vanmaekelbergh, D.; Donega, C. de M.; Highly emissive divalent-ion-doped colloidal CsPb1-xMxBr3 perovskite nanocrystals through cation exchange, *J. Am. Chem. Soc.* **2017**, 139, 4087-4097.

(12) Begum, R.; Parida, M. R.; Abdelhady, A.L.; Murali, B.; Alyami, N. M.; Ahmed, G. H.; Hedhili, M. N.; Bakr, O.M.; Mohammed, O.F. Engineering interfacial charge transfer in CsPbBr3 perovskite nanocrystals by heterovalent doping, *J. Am. Chem. Soc*. **2017**, 139, 731-737.

(13) Zhang, X.; Zhang, Y.; Zhang, X.; Yin, W.; Wang, Y.; Wang, H.; Lu, M.; Li, Z.; Gu. Z.; Yu. W. W. Yu, Yb3þ and Yb3þ/Er3þ doping for near-infrared emission and improved stability of CsPbCl3 nanocrystals, *J. Mater. Chem. C.* **2018**, 6, 10101-10105.

(14) Liu, M.; Zhong, G.; Yin, Y.; Miao, J.; Li, K.; Wang, C.; Xu, X.; Shen, C.; Meng, H. Aluminum-doped cesium lead bromide perovskite nanocrystals with stable blue photoluminescence used for display backlight, *Adv. Sci,* **2017**, 4, 1700335.

(15) Lu, M.; Zhang, X.; Bai, X.; Wu, H.; Shen, X.; Zhang, Y.; Zhang, W.; Zheng, W.; Song, H.; Yu, W. W.; Rogach, A.L. Spontaneous silver doping and surface passivation of CsPbI3 perovskite active layer enable light-emitting devices with an external quantum efficiency of 11.2%, *ACS Energy Lett.* **2018**, 3, 1571-1577.

(16) Yao, J.; Ge, J.; Han, B.; Wang, K.; Yao, H.; Yu, H.; Li, J.; Zhu, B.; Song, J.; Chen, C.; Zhang, Q.; Zeng, H.; Luo, Y.; Yu, S.; Ce3þ-doping to modulate photoluminescence kinetics for efficient CsPbBr3 nanocrystals based light-emitting diodes, *J. Am. Chem. Soc.* **2018**, 140, 3626-3634.

(17) Xu, L.; Yuan, S.; Zeng, H.; Song. J. A comprehensive review of doping in perovskite nanocrystals/quantum dots: evolution of structure, electronics, optics and light-emitting diodes. *Materials Today Nano.* **2019**, 6, 100036.

(18) Kanwat, A.; Choi, W. C.; Seth, S.; Jang, J.; Doping and Photon Induced Defect Healing of Hybrid Perovskite Thin Films: An Approach Towards Efficient Light Emitting Diodes, *CHEMNANOMAT*. **2019**, 5(5), 666-673,

(19) Wu, C. Zou, Y.; Wu, T.; Ban, M.; Pecunia, V.; Han, Y.; Liu, Q.; Song, T.; Duhm, S.; Sun, B.; *Adv. Funct. Mater.* **2017**, 27, 1700338.

(20) Song, L., Guo, X., Hu, Y.; Lv, Y.; Lin, J.; Liu, Z.; Fan, Y.; Liu, X.; *J. Phys. Chem. Lett.* **2017**, 8, 4148.

(21) Lee, S.; Park, J. H.; Nam, Y. S.; Lee, B. R.; Zhao, B.; Nuzzo, D. D.; Jung, E. D.; Jeon, H.; Kim, J. Y.; Jeong, H. Y.; Friend, R. H.; Song, M. H.; *ACS Nano*. **2018**, 12, 3417.

(22) Zou, Y.; Ban, M.; Yang, Y.; Bai, S.; Wu, C.; Han, Y.; Wu, T.; Tan, Y.; Huang, Q.; Gao, X.; Song, T.; Zhang, Q.; Sun, B. *ACS Appl. Mater. Interfaces*. **2018**, 10, 24320.

(23) Han, D.; Imran, M.; Zhang, M.; Chang, S.; Wu, X. G.; Zhang, X.; Tang, J.; Wang, M.; Ali, S.; Li, X.; Yu, G.; Han, J.; Wang, L.; Zou, B.; Zhong, H.; *ACS Nano*. **2018**, 12, 8808.

(24) Lee, S.; Kim, D. B.; Yu, J. C.; Jang, C. H.; Park, J.H.; Lee, B.R.; Song, M. H. Versatile Defect Passivation Methods for Metal Halide Perovskite Materials and their Application to Light-Emitting Devices, *Adv.Mater.* **2019**, 31, 1805244

(25) Chin, X Y ; Perumal, A ; Bruno, A ; Yantara, N ; Veldhuis, SA ; Martinez-Sarti, L ; Chandran, B ; Chirvony, V ; Lo, ASZ ; So, J ; Soci, C ; Gratzel, M ; Bolink, HJ ; Mathews, N ; Mhaisalkar, S G Self-assembled hierarchical nanostructured perovskites enable highly efficient LEDs via an energy cascade *Energy Environ. Sci.* **2018**, 11, 7, 1770-1778

(26) Quan, L. N.; Zhao, Y.; García de Arquer, F. P.; Sabatini, R.; Walters, G.; Voznyy, O.; Comin, R.; Li, Y.; Fan, J. Z.; Tan, H.; et al. Tailoring the Energy Landscape in Quasi-2D Halide Perovskites Enables Efficient Green-Light Emission. *Nano Lett.* **2017**, 17 (6), 3701−3709.

(27) Yuan, M.; Quan, L. N.; Comin, R.; Walters, G.; Sabatini, R.; Voznyy, O.; Hoogland, S.; Zhao, Y.; Beauregard, E. M.; Kanjanaboos, P.; Lu, Z.; Kim, D. H.; Sargent, E. H. Perovskite Energy Funnels for Efficient Light-Emitting Diodes. *Nat. Nanotechnol.* **2016**, 11, 872.

(28) Ng, Y. F.; Kulkarni, S. A.; Parida, S.; Jamaludin, N. F.; Yantara, N.; Bruno, A.; Soci, C.; Mhaisalkar, S.; Mathews, N. Highly efficient Cs-based perovskite light-emitting diodes enabled by energy funnelling. *Chem. Commun.* **2017**, 53, 12004−12007..

(29) Yang, X.; Zhang, X.; Deng, J.; Chu, Z.; Jiang, Q.; Meng, J.; Wang, P.; Zhang, L.; Yin, Z.; You, J. Efficient Green Light-emitting Diodes Based on Quasi-two-dimensional Composition and Phase Engineered Perovskite with Surface Passivation. *Nat. Commun.* **2018**, 9, 570.

(30) Wang, N.; Cheng, L.; Ge, R.; Zhang, S.; Miao, Y.; Zou, W.; Yi, C.; Sun, Y.; Cao, Y.; Yang, R.; et al. Perovskite Light-Emitting Diodes Based on Solution-Processed Self-Organized Multiple Quantum Wells. *Nat. Photonics* **2016**, 10, 699−704.

(31) Zhang, S.; Yi, C.; Wang, N.; Sun, Y.; Zou, W.; Wei, Y.; Cao, Y.; Miao, Y.; Li, R.; Yin, Y.; Zhao, N.; Wang, J.; Huang, W. Efficient red perovskite light-emitting diodes based on solution-processed multiple quantum Wells. *Adv. Mater.* **2017**, 29, 1606600

(32) Zou, W.; Li, R.; Zhang, S.; Liu, Y.; Wang, N.; Cao, Y.; Miao, Y.; Xu, M.; Guo, Q.; Di, D.; et al. Minimising Efficiency Roll-off in HighBrightness Perovskite Light-Emitting Diodes. *Nat. Commun.* **2018**, 9, 608.

(33) Si, J.; Liu, Y.; He, Z.; Du, H.; Du, K.; Chen, D.; Li, J.; Xu, M.; Tian, H.; He, H.; Di, D.; Lin, C.; Cheng, Y.; Wang, J.; Jin, Y. Efficient and High-Color-Purity Light-Emitting Diodes Based on In Situ Grown Films of CsPbX3 (X = Br, I) Nanoplates with Controlled Thicknesses. *ACS Nano.* **2017**, 11, 11100−11107

(34) Kanwat, A.; Moyen, E.; Cho, S.; Jang, J. Rubidium as an Alternative Cation for Efficient Perovskite Light-Emitting Diodes. *ACS Appl. Mater. Interfaces* **2018**, 10 (19), 16852−16860

(35) Zirak, M.; Moyen, E.; Alehdagi, H.; Kanwat, A.; Choi, W. C.; Jang, J. Anion- and Cation-Codoped All-Inorganic Blue-Emitting Perovskite Quantum Dots for Light-Emitting Diodes, *ACS Appl. Nano Mater.* **2019**, 2, 9, 5655-5662
(36) Linaburg, M. R.; McClure, E. T.; Majher, J. D.; Woodward, P. M. Cs1−xRbxPbCl3 and Cs1−xRbxPbBr3 Solid Solutions: Understanding Octahedral Tilting in Lead Halide Perovskites. *Chem. Mater.* **2017**, 29 (8), 3507−3514.
(37) Abdi-Jalebi, M.; Andaji-Garmaroudi, Z.; Cacovich, S.; Stavrakas, C.; Philippe, B.; Richter, J. M.; Alsari, M.; Booker, E. P.; Hutter, E. M.; Pearson, A. J.; Lilliu, S.; Savenije, T. J.; Rensmo, H.; Divitini, G.; Ducati, C.; Friend, R. H.; Stranks, S. D. Maximizing and Stabilizing Luminescence from Halide Perovskites with Potassium Passivation. *Nature* **2018**, 555, 497−501.
(38) Kubicki, D. J.; Prochowicz, D.; Hofstetter, A.; Zakeeruddin, S. M.; Gratzel, M.; Emsley, L. Phase Segregation in Potassium-Doped¨ Lead Halide Perovskites from 39K Solid-State NMR at 21.1 T. *J. Am. Chem. Soc.* **2018**, 140, 7232−7238
(39) Zheng, F.; Chen, W.; Bu, T.; Ghiggino, K. P.; Huang, F.; Cheng, Y.; Tapping, P.; Kee, T. W.; Jia, B.; Wen, X. Triggering the Passivation Effect of Potassium Doping in Mixed-Cation Mixed Halide Perovskite by Light Illumination. *Adv. Energy Mater*. **2019**, No. 1901016.
(40) Kieslich, G.; Sun, S. J. Cheetham, A. K. An extended Tolerance Factor approach for organic-inorganic perovskites. *Chem. Sci.* **2015**, 6, 3430– 3433,
(41) Wright, A. D.; Verdi, C.; Milot, R. L.; Eperon, G. E.; Perez-´ Osorio, M. A.; Snaith, H. J.; Giustino, F.; Johnston, M. B.; Herz, L. M. Electron−phonon coupling in hybrid lead halide perovskites. *Nat. Commun.* **2016**, 7, 11755.
(42) Filip, M. R.; Eperon, G. E.; Snaith, H.; Giustino, F. Steric Engineering of Metal-Halide Perovskites with Tunable Optical Band Gaps. *Nat. Commun*. **2014**, 5, 5757.
(43) Kubicki, D. J.; Prochowicz, D.; Hofstetter, A.; Zakeeruddin, S. M.; Grätzel, M.; Emsley, L. Phase Segregation in Cs-, Rb- and K-Doped Mixed-Cation $(MA)_x(FA)_{1-x}PbI_3$ Hybrid Perovskites from Solid-State NMR, *J. Am. Chem. Soc.* **2017**, 139, 40, 14173-14180
(44) Kubicki, D. J.; Prochowicz, D.; Hofstetter, A.; Zakeeruddin, S. M.; Grätzel, M.; Emsley, L. Phase Segregation in Potassium-Doped Lead Halide Perovskites from ^{39}K Solid-State NMR at 21.1 T, J. Am. Chem. Soc. **2018**, 140, 7232−7238
(45) Jalebi, M. A.; Garmaroudi, Z. A.; Pearson, A. J.; Divitini, G.; Cacovich, S.; Philippe, B.; Rensmo, H.; Ducati, C.; Friend, R. H.; Stranks, S. D. Potassium- and Rubidium-Passivated Alloyed Perovskite Films: Optoelectronic Properties and Moisture Stability. *ACS Energy Lett.* **2018**, 3, 11, 2671-2678
(46) Hu, Y.; Aygüler, M. F.; Petrus, M. L.; Bein, T.; Docampo, P. Impact of Rubidium and Cesium Cations on the Moisture Stability of Multiple-Cation Mixed-Halide Perovskites, *ACS Energy Lett.* **2017**, 2, 10, 2212-2218.
(47) Bu, T.; Liu, X.; Zhou, Y.; Yi, J.; Huang, X.; Luo, L.; Xiao, J.; Ku, Z.; Peng, Y.; Huang, F.; et al. A Novel Quadruple-cation Absorber for Universal Hysteresis Elimination for High Efficiency and Stable Perovskite Solar Cells. *Energy Environ. Sci.* **2017**, 10, 2509−2515.
(48) Futscher, H. M.; Lee, J. M.; McGovern, L.; Muscarella, L. A.; Wang, T.; Haider, M. I.; Fakharuddin, A.; Mende, L. S.; Ehrler, B. Quantification of ion migration in CH3NH3PbI3 perovskite solar cells by transient capacitance Measurements, ***Mater. Horiz.***, 2019,**6**, 1497-1503
(49) Li, C.; Guerrero, A.; Zhong, Y.; Graser, A.; Luna, C. A. M.;¨ Köhler, J.; Bisquert, J.; Hildner, R.; Huettner, S. Real-Time Observation of Iodide Ion Migration in Methylammonium Lead Halide Perovskites. *Small* **2017**, 13, 1701711

(50) Franssen, W. M. J.; Kentgns, A. P. M.Solid–state NMR of hybrid halide perovskites, Solid State Nuclear Magnetic Resonance, 2019, 100, 36-34
(51) Bernard, G. M.; Wasylishen, R.; Ratcliffe, C. I.; Terskikh, V.; Wu, Q.; Buriak, J. M.; Hauger, T. Methylammonium Cation Dynamics in Methylammonium Lead Halide Perovskites: A Solid-State NMR Perspective, *J. Phys. Chem. A,* **2018**, 122, 6, 1560-1573.
(52) Roiland, C.; Allard, G. T.; Jemli, K.; Alonso, B.; Ameline, J. C.; Gautier, R.; Bataille, T.; Pollès, L. T.; Deleporte, Even, J.; Katan, C.; Multinuclear NMR as a tool for studying local order and dynamics in $CH_3NH_3PbX_3$ (X = Cl, Br, I) hybrid perovskites, ***Phys. Chem. Chem. Phys.*** **2016**, **18**, 27133-27142
(53) Baikie, T.; Barrow, N. S.; Fang, Y.; Keenan, P. J.; Slater, P. R.; Piltz, R. O.; Gutmann, M.; Mhaisalkar, S. G.; White, T. M.; A combined single crystal neutron/X-ray diffraction and solid-state nuclear magnetic resonance study of the hybrid perovskites $CH_3NH_3PbX_3$ (X = I, Br and Cl), ***J. Mater. Chem. A***, **2015**, **3**, 9298-9307
(54) Rosales, B. A.; Men, L.; Cady, S. D.; Hanrahan, M. P.; Rossini, A. J.; Vela, J. Persistent Dopants and Phase Segregation in Organolead Mixed-Halide Perovskites, *Chem. Mater.* , 28, 19, 6848-6859

(55) Karmakar, A.; Dodd, M. S.; Zhang, X.; Oakley, M. S.; Klobukowski, M.; and Michaelis, V. K., Mechanochemical synthesis of 0D and 3D cesium lead mixed halide perovskites, **Chem. Commun.** *2019, **55**, 5079-5082.*
(56) Ray, A.; Maggioni, D.; Baranov, D.; Dang, Z.; Prato, M.; Akkerman, Q. A.; Goldoni, L.; Caneva, E.; Manna, L.; Abdelhady, A. L. Green-Emitting Powders of Zero-Dimensional Cs4PbBr6: Delineating the Intricacies of the Synthesis and the Origin of Photoluminescence. Chem. Mater. **2019**, 31, 7761−7769.
(57) Yunhua Chen, Smock, S. R; Flintgruber, A. H.; Perras, F. A.; Brutchey, R. L.; and Rossini. A. j. The Surface Termination of CsPbBr3 Perovskite Quantum Dots Determined by Solid-State NMR Spectroscopy, *J. Am. Chem. Soc.* **2020**, 142, 13, 6117-6127.
(58) Cao, J.; Tao, S. X.; Bobbert, P. A.; Wong, C.-P.; Zhao, N. Interstitial Occupancy by Extrinsic Alkali Cations in Perovskites and Its Impact on Ion Migration. *Adv. Mater***.** **2018**, 30, 1707350.
(59) Quan, L. N.; Quintero-Bermudez, R.; Voznyy, O.; Walters, G.; Jain, A.; Fan, J. Z.; Zheng, X.; Yang, Z.; Sargent, E. H. Highly emissive green perovskite nanocrystals in a solid state crystalline matrix. *Adv. Mater.* **2017**, *29*, 1605945
(60) de Weerd, C.; Lin, J.; Gomez, L.; Fujiwara, Y.; Suenaga, K.; Gregorkiewicz, T. Hybridization of Single Nanocrystals of Cs4PbBr6 and CsPbBr3. J. Phys. Chem. C **2017**, 121 (35), 19490−19496
(61) Wang, L.; Liu, L.; Zhang, Y.; and Mohammed, O. F., Photoluminescence Origin of Zero Dimensional Cs4PbBr6 Perovskite, ACS Energy Lett. **2020**, 5, 87−99
(62) Xiao, C.; Li, Z.; Guthrey, H.; Moseley, J.; Yang, Y.; Wozny, S.; Moutinho, H.; To, B.; Berry, J. J.; Gorman, B.; Yan, Y.; Zhu, K.; AlJassim, M. J. Mechanisms of Electron-Beam-Induced Damage in Perovskite Thin Films Revealed by Cathodoluminescence Spectroscopy, *Phys. Chem. C **2015**, 119 (48), 26904−26911.*
(63) Rothmann, M. U.; Li, W.; Etheridge, J.; Cheng, Y. B. Microstructural Characterisations of Perovskite Solar Cells – From Grains to Interfaces: Techniques, Features, and Challenges*, Adv. Energy Mater. **2017**, 7, 1700912*
(64) Anaya, M.; Rand, B. P.; Holmes, r. j.; Credgington, D.; Bolink, H. J.; Friend, R. H.; Wang, J.; Greenham, N. C.; Stranks, S. D. Best practices for measuring emerging light-emitting diode technologies, *Nature Photonics*, **2019** 13, 818–821.
(65) Li, C.; Wang, N.; Guerrero, A.; Zhong, Y.; Long, H.; Miao, Y.; Bisquert, J.; Wang, J.; Huettner, S. Understanding the Improvement of Stability in Self-Assembled Multiple

Quantum Wells Perovskite Light-Emitting Diode. *J. Phys. Chem. Lett.* **2019**, 10, 6857−6864.

Supporting Information

Electroluminescence of Halide Perovskites with Potassium Passivation

*Anil Kanwat, Natalia Yantara, Yan Fong Ng, Thomas J. N. Hooper, Prem Jyoti Singh Rana, Benny Febriansyah, Padinhare Cholakkal Harikesh, Teddy Salim, Parth Vashishtha, Subodh G. Mhaisalkar, and Nripan Mathews**

Films and device Characterization:

The XRD measurements were performed with Bruker D8 Advance X-ray diffractometer using Ni-filtered Cu Kα radiation.

The absorption spectra were recorded using UV-Vis-NIR spectrophotometer (UV-3600, Shimadzu) equipped with an integrating sphere.

The steady state PL spectra were measured using Fluoromax-4 (Horiba Jobin Yvon) spectrofluorometer at an excitation wavelength of 350 nm.

The FESEM imaging of perovskite films (on ITO/PEDOT:PSS substrates) was performed using a JEOL JSM-7600F scanning electron microscope at 5-10 kV with a working distance of ~8 mm.

A JEOL 2100F was used for the HR-TEM analyses at an accelerating voltage of 200 kV and beam current of 146 μA. Samples were prepared by spin coating the precursor solution on carbon support copper grids. To collect the HRTEM micrograph, the perovskite samples were exposed not more than 10 seconds to minimize beam damage.

Capacitance–voltage (C–V) measurements were carried out at 200 kHz in Autolab PGSTAT302N. The measurements were done under dark at an AC voltage of 20mV at room temperature.

Auger electron spectroscopy (AES) was performed with a field-emission Auger microprobe (JEOL JAMP-7830F) with a primary electron beam having an accelerating voltage of 10 keV and a probe current of 10 nA. The sample was tilted at 55° throughout the analysis. Auger mapping was collected from an area of 5x5 um^2 corresponding to magnification of 300x, with a dwell time of 5 ms and averaged over 10 accumulations for Cs/Br and 1 accumulation for K. The analyser was operated at a constant retarding

ratio (CRR) mode (energy resolution < 0.5%) for both spectroscopy and mapping. The surface composition was determined by considering the peak-to-peak distance of the differentiated Auger spectra and the relative sensitive factor (RSF) for the elements of interest, i.e., K, Cs, and Br.

All solid state NMR experiments in this study were completed on a 14.1 T Bruker Avance III HD 600 MHz spectrometer with a Bruker 4mm HX MAS probe operating at an MAS frequency of 14 KHz. The ^{133}Cs NMR ($\upsilon_0(^{133}Cs)$ = 78.73 MHz) experiments employed a one-pulse sequence, utilising a selective $\pi/2$ pulse of 7.5 μs (determined on $CsCl_{(s)}$) and a recycle delay of 1025 s. The resulting data was referenced with respect to 0.1 M $CsNO_{3(aq)}$ (δ_{iso} = 0 ppm). The ^{133}Cs spin-lattice relaxation times (T_1) were determined using a saturation recovery pulse sequence with a 200 pulse saturation pulse train. The ^{207}Pb NMR ($\upsilon_0(^{207}Pb)$ = 125.55 MHz) experiments employed a Hahn-echo pulse sequence, utilising $\pi/2$ and π pulses of 5.0 and 10.0 μs (determined on 1.1 M $Pb(NO_3)_{2(aq)}$), a recycle delay of 10 s, and a rotor synchronised echo delay of 63.9 μs. The resulting data was referenced with respect to 1.1 M $Pb(NO_3)_{2(aq)}$ (δ_{iso} = −2965.7 ppm). The ^{79}Br NMR ($\upsilon_0(^{79}Br)$ = 150.38 MHz) experiments employed a one-pulse sequence, utilising a selective $\pi/2$ pulse of 3.6 μs (determined on $KBr_{(s)}$) and a recycle delay of 0.25 s. The resulting data was referenced with respect to 0.01 M $NaBr_{(aq)}$ (δ_{iso} = 0 ppm). Spectra simulation was performed using the DMFit software package (Ref. 10.1002/mrc.984).

The electrical poling was performed using the same Keithley 2612B by applying a fixed constant bias (1, 2 and 3 V) for a set duration of 1 min.

All PeLED devices were tested at ambient conditions. The characteristic current density–voltage–luminance (J-V-L) were recorded with a Keithley 2612B source meter and an OceanOptics QE Pro spectrometer connected to an integrating sphere and operated using Ciemo LabVIEW software.

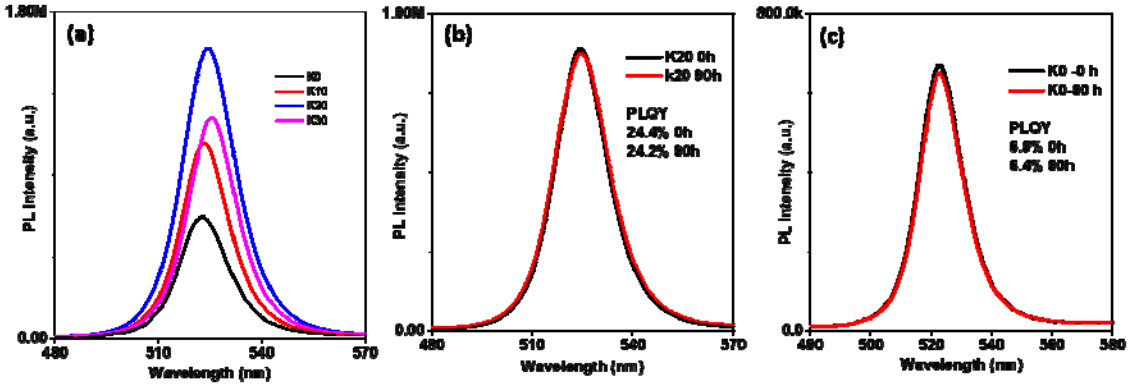

FIG. S1 (a) Photoluminescence intensity with increasing K^+ concentration in KBr mixed $CsPbBr_3$ films; K0, K10, K20, and K30. The PL intensity increases 1.6, 1.8, and 2.4 fold with respect to K0 in K10, K20, and K30, respectively. PL and PLQY stability for 90 hr of (b) K20, and (c) K0 perovskite films.

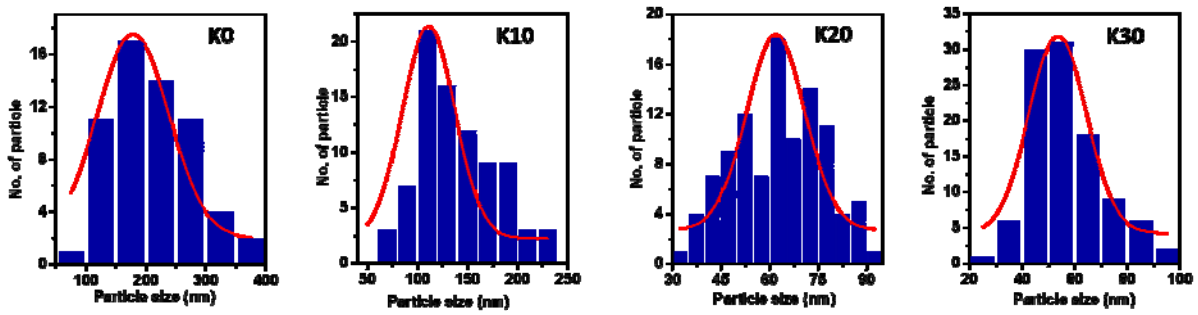

FIG. S2 Histogram of crystallite size calculated from field emission scanning electron microscopy (FIG 2) of perovskite films with increasing KBr concentration; K0, K10, K20, and K30.

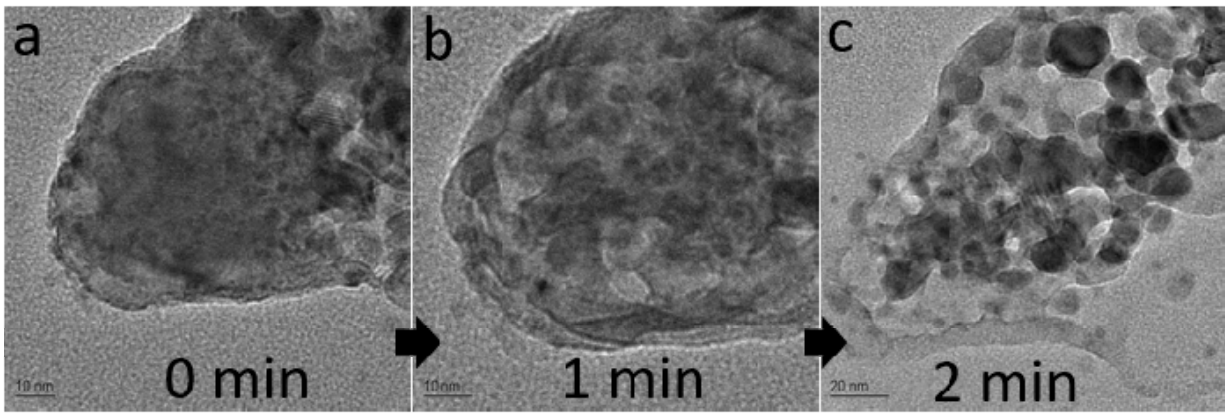

FIG. S3 HR-TEM images of K20 sample with increasing electron beam exposure time on the specimen for (a) 0 min (b) 1 min, and (c) 2 min.

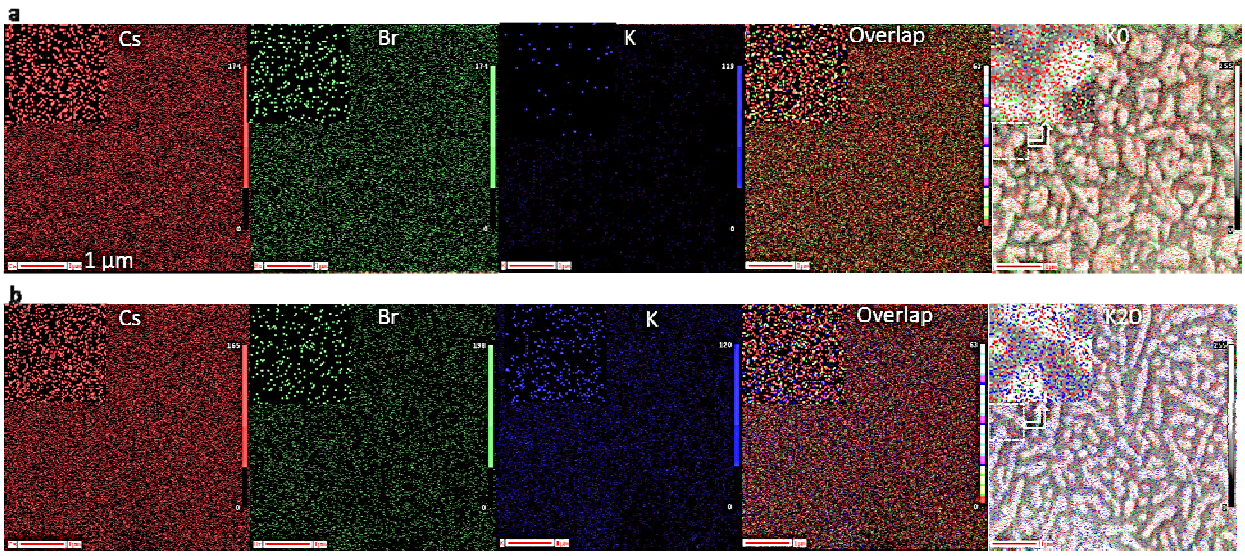

FIG. S4 Auger electron spectroscopy (AES) of (a) K0 (unmodified) and (b) K20 (KBr modified) films. The inset depicts the zoomed AES elemental mapping of Cs, Br, K, and overlapped area of these elements.

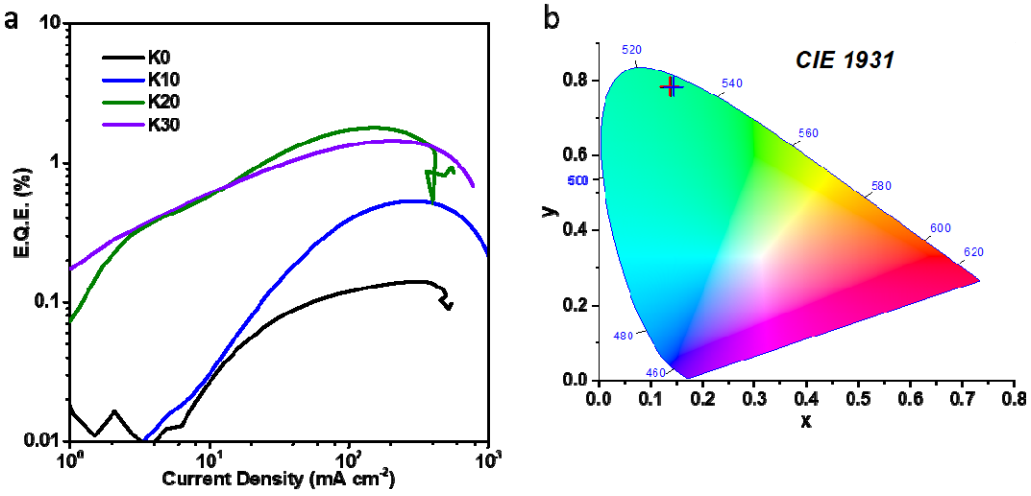

FIG. S5 (a) EQE, and (b) CIE- co-ordinate of PeLEDs with increasing KBr concentration.

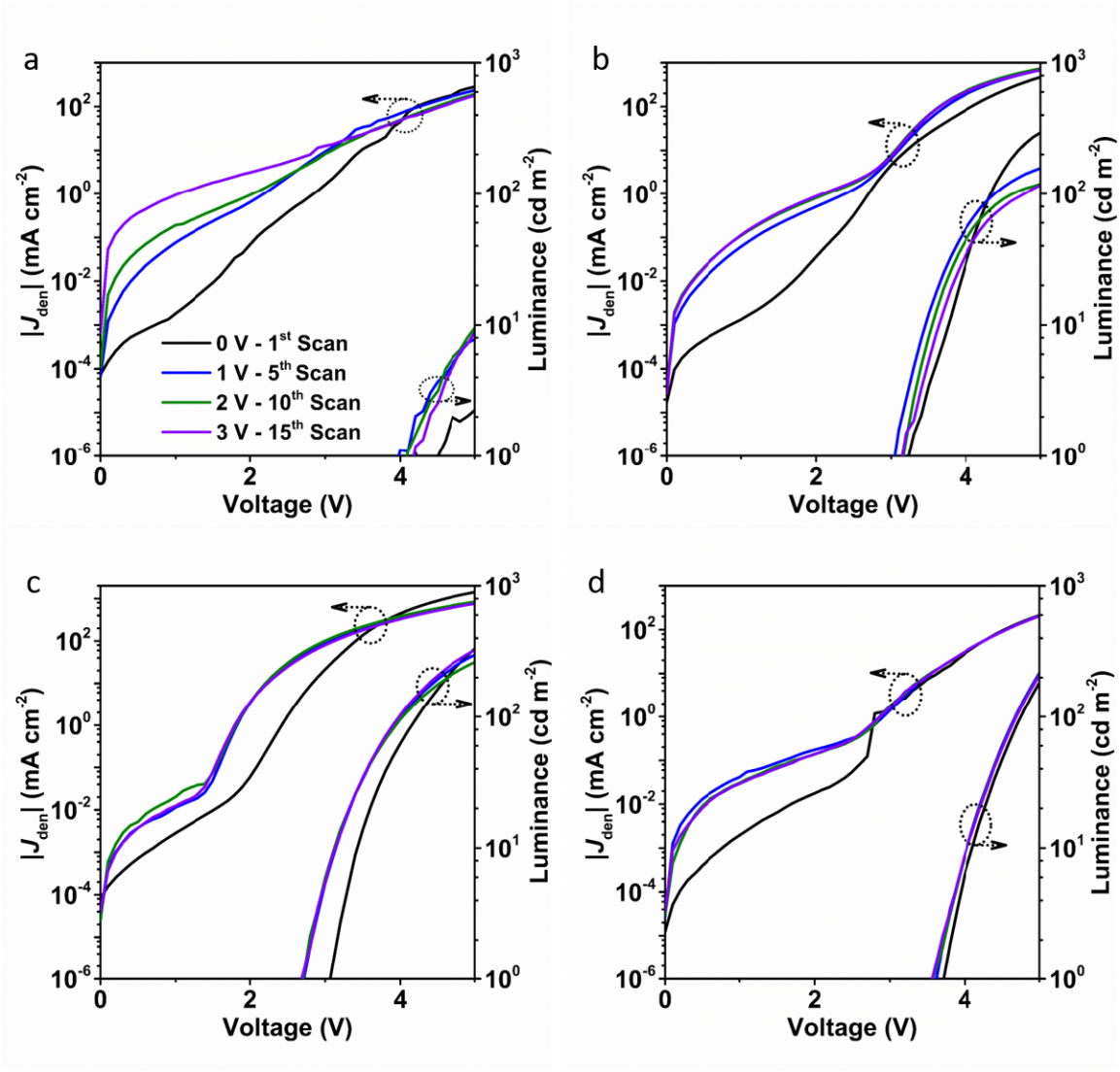

FIG. S6 J-V-L plots before (0) and after electrical poling at 1 V, 2 V, and 3 V with increasing KBr concentration; (a) K0, (b) K10, (c) K20, and (d) K30.

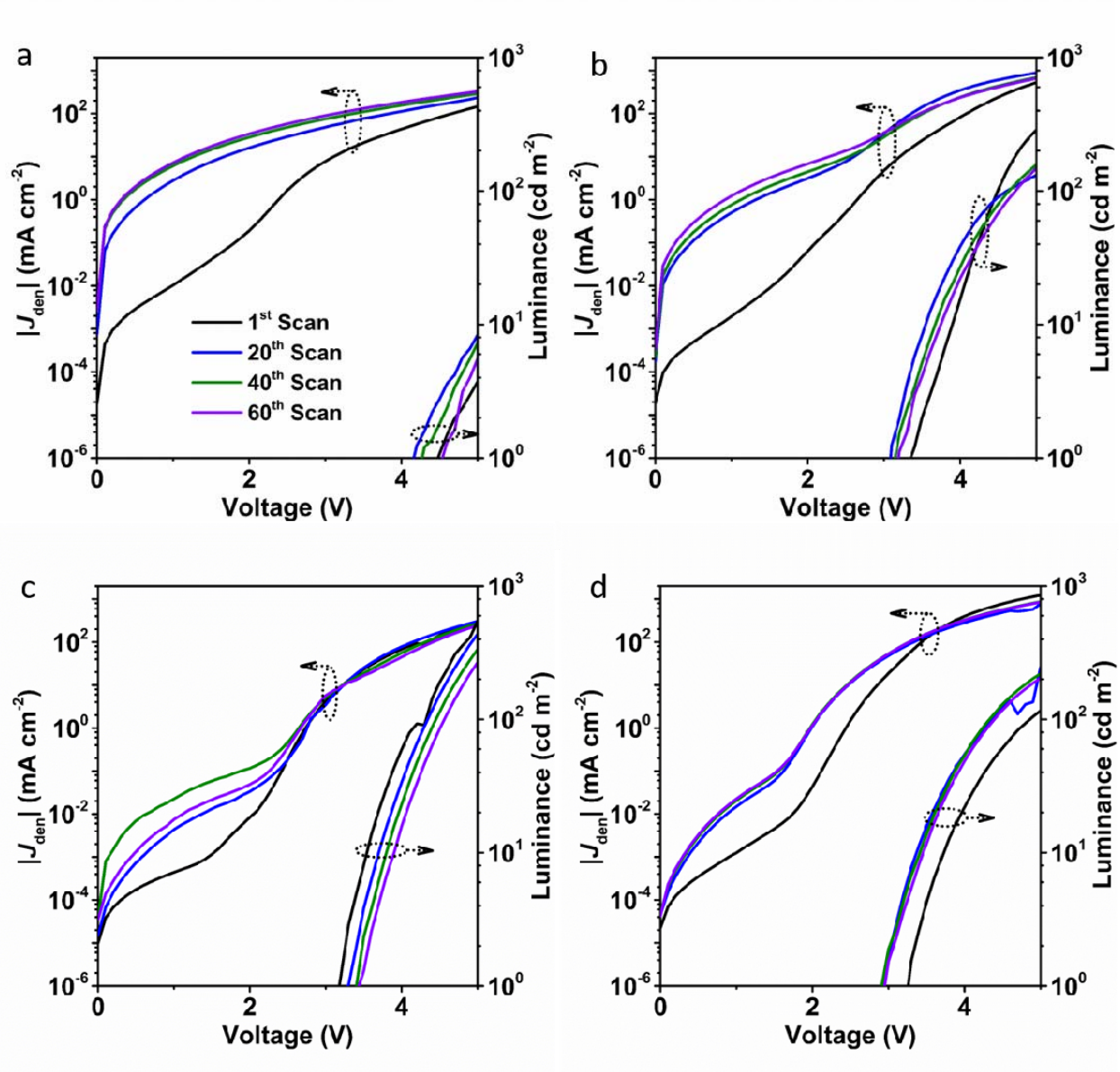

FIG. S7 J-V-L plots with multiple scan of PeLED devices from 0-5V with increasing KBr concentration; (a) K0, (b) K10, (c) K20, and (d) K30.

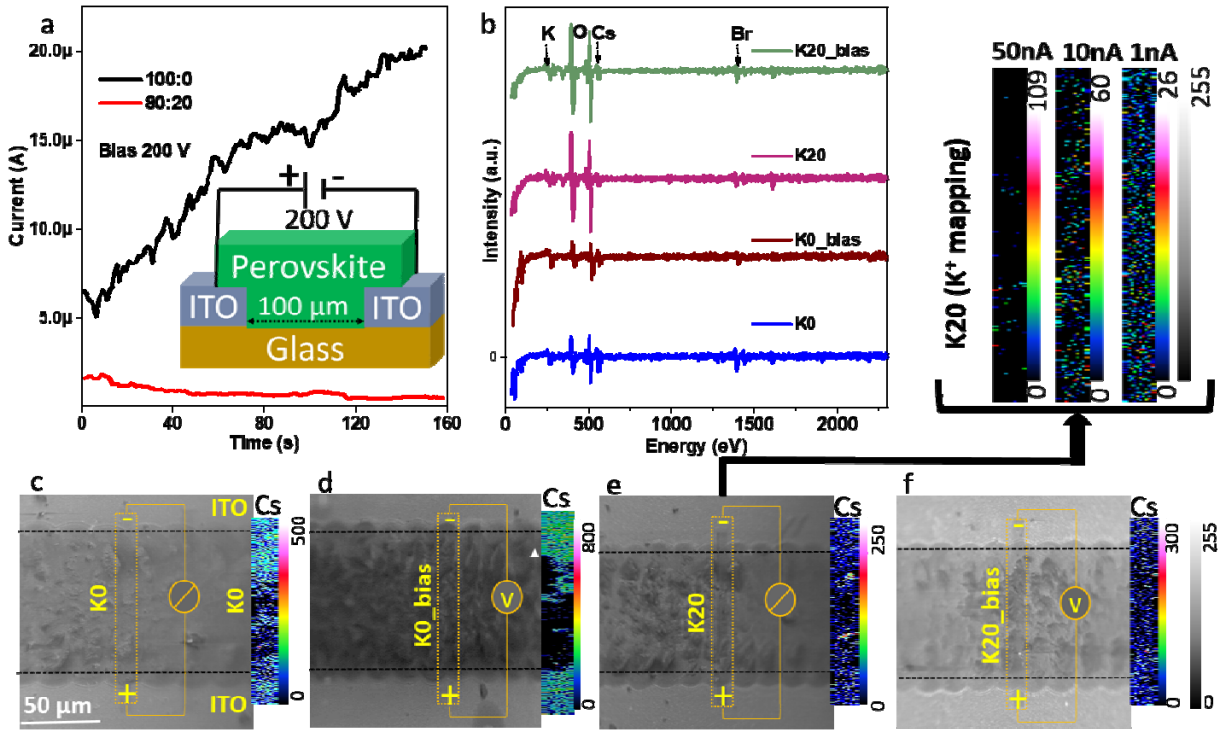

FIG. S8 (a) Current plots of K0 (unmodified) and K20 (KBr modified) films at applied constant bias of 200V for 150 sec. The inset depicts the device preparations for Auger electron spectroscopy (AES). (b) AES full scan of K0 and K20 perovskite films before and after applied bias. Cs^+ mapping of (c,d) K0 and (e,f) K20 perovskite films before (c,e) and after (d,f) applied bias. Extended figure of (e) depicts K^+ elemental mapping with decreasing Auger current from 50 nA to 1nA.

Table S1. The ^{133}Cs NMR parameters of the K0, and K20 thin film samples determined via Gaussian/Lorentzian fitting and saturation recovery relaxation experiments.

Sample	Assignment	$\delta_{iso}(^{133}Cs)$ (ppm)	FWHM (KHz)	T_1 relaxation (s)	Relative intensity (%)
K0	$CsPbBr_3$	117.6 ± 0.6	0.36 ± 0.04	175 ± 8	59
	Cs_4PbBr_6	235.5 ± 0.9	0.57 ± 0.07	190 ± 20	41
K20	$CsPbBr_3$	117.6 ± 0.6	0.36 ± 0.04	160 ± 10	32
	Cs_4PbBr_6	239 ± 3	2.3 ± 0.3	200 ± 60	68

Table S2: The ^{207}Pb NMR parameters of the K0 and K20 thin film samples determined via *J*-coupling spectral simulation.

Sample	**Assignment**	**δ_{iso}(^{207}Pb)** (ppm)	**FWHM** (KHz)	**^{1}J(^{207}Pb – $^{79/81}$Br)** (KHz)	**Relative intensity** (%)
K0	$CsPbBr_3$	269 ± 3	2.6 ± 0.3	2.3 ± 0.3	83
	Cs_4PbBr_6	−349 ± 2	1.5 ± 0.2	2.0 ± 0.2	17
K20	$CsPbBr_3$	270 ± 3	2.8 ± 0.3	2.3 ± 0.3	62
	Cs_4PbBr_6	−366 ± 4	>4	2.0	38